

Article

Oxygen Reduction Reaction Catalyzed by Pt₃M (M = 3d Transition Metals) Supported on O-doped Graphene

Chaonan Cui ^{1,2,3}, Mengnan Sun ¹, Xinli Zhu ¹, Jinyu Han ¹, Hua Wang ^{1,2,*}  and Qingfeng Ge ^{2,*} 

¹ Key Laboratory for Green Chemical Technology of the Ministry of Education, School of Chemical Engineering and Technology, Collaborative Innovation Center of Chemical Science and Engineering, Tianjin University, Tianjin 300072, China; chncui@tju.edu.cn (C.C.); mengnans@tju.edu.cn (M.S.); xinlizhu@tju.edu.cn (X.Z.); hanjinyu@tju.edu.cn (J.H.)

² Department of Chemistry and Biochemistry, Southern Illinois University, Carbondale, IL 62901, USA

³ State Key Laboratory for Structural Chemistry of Unstable and Stable Species, Institute of Chemistry, Chinese Academy of Sciences, Beijing 100190, China

* Correspondence: tjuwanghua@tju.edu.cn (H.W.); qge@chem.siu.edu (Q.G.); Tel.: +1-618-453-6406 (Q.G.)

Received: 27 December 2019; Accepted: 16 January 2020; Published: 1 February 2020



Abstract: Pt₃M (M = 3d transition metals) supported on oxygen-doped graphene as an electrocatalyst for oxygen reduction was investigated using the periodic density functional theory-based computational method. The results show that oxygen prefers to adsorb on supported Pt₃M in a bridging di-oxygen configuration. Upon reduction, the O–O bond breaks spontaneously and the oxygen adatom next to the metal–graphene interface is hydrogenated, resulting in co-adsorbed O* and OH* species. Water formation was found to be the potential-limiting step on all catalysts. The activity for the oxygen reduction reaction was evaluated against the difference of the oxygen adsorption energy on the Pt site and the M site of Pt₃M and the results indicate that the oxygen adsorption energy difference offers an improved prediction of the oxygen reduction activity on these catalysts. Based on the analysis, Pt₃Ni supported on oxygen-doped graphene exhibits an enhanced catalytic performance for oxygen reduction over Pt₄.

Keywords: oxygen reduction reaction; Pt-based catalyst; adsorption energy; transition metals

1. Introduction

Proton-exchange membrane fuel cells (PEMFCs) can directly convert the chemical energy stored in hydrogen and oxygen into electricity [1–3], but their adoption for practical application as electrocatalysts is hindered by the high price and limited supply of platinum [4–6]. Efforts have been made to reduce, and even replace, platinum in electrocatalysts. Alloying platinum with inexpensive metals has been shown to maintain or improve the activity for the oxygen reduction reaction (ORR) while significantly reducing the cost [7–12]. Among inexpensive metals, 3d metals, including Ti [13,14], V [13,14], Cr [14], Mn [14], Fe [13–16], Co [13–15,17,18], Ni [13–15,19], and Cu [17,20,21] have been tested as a component of the electrocatalysts for ORR.

Graphitic carbon materials have long been used as electrode materials, with graphene-based materials being natural alternatives due largely to their generally high electrical conductivity, high specific surface areas, and strong chemical strength [22,23]. Therefore, graphene-supported Pt and metal alloy catalysts have been studied for the oxygen reduction process [24–26]. B-, N-, and S-doped graphene have also been investigated for ORR [27–31]. Various functional groups on graphene have been reported to enhance the ORR activity [32]. In particular, graphene oxides and oxygen-containing

graphene materials are widely available. These oxygen-derived defect sites in graphene may form the anchor sites for the active catalyst and/or work synergistically with the active components to promote the reactions. Consequently, the use of graphene oxides either alone or as a support in the electrode has attracted extensive attention [6,33–35]. In the present study, we use O-doped graphene to model the oxygen-containing graphene materials.

Our previous study on the ORR process over Pt₄, Pt₃V, and Pt₃Fe supported on O-doped graphene showed that V and Fe change the ORR mechanism and activity on the Pt-based catalysts differently [36]. Other studies also reported that early and late 3d transition metals could affect the adsorption of O₂ and the ORR activity in a different way [13,37]. Herein, we examined the entire row of 3d transition metals in the form of Pt₃M with M = Sc, Ti, V, Cr, Mn, Fe, Co, and Ni on O-doped graphene (OG) as the ORR catalysts. We compared the effect of transition metals on the ORR mechanism and activity. Through a detailed analysis of O₂, OH, and H₂O adsorption energies, as well as the ORR mechanism, we identified Ni as the most effective modifier.

2. Results and Discussion

2.1. Optimized Pt₃M Structures on O-doped Graphene

Our previous study showed that the O-doping site is the anchoring site for the tetrahedral Pt₄ cluster [36]. The OG-supported Pt₃M clusters (OG-Pt₃M) were constructed by replacing one Pt atom of the supported Pt₄ cluster with M at either the interfacial or the top of tetrahedron. Structural optimization showed that the interfacial substituted Pt₃M cluster is more stable, which was used for the ORR study. In this work, we expanded M to include all 3d metals, i.e., M = Sc, Ti, V, Cr, Mn, Fe, Co, and Ni. As we showed previously, the doped O atom is 2-C coordinated and 0.72 Å above the plane of the graphene sheet on pure OG [38]. As shown in Table 1, the doped O atom was pushed to the opposite side of the graphene sheet at a distance of 0.17–0.60 Å, depending on M in the supported cluster. The details of the optimized structures are shown in Table S1 of the Supporting Information.

Table 1. Bader charges of the metal atoms, doped oxygen and the carbon atoms bonded with oxygen, and the distance between the doped oxygen atom and the graphene plane ($d_{(O-OG)}$ in Å). The corresponding atoms are labeled in the accompanying structures under the table.

Cluster		Pt ₄	Pt ₃ Sc	Pt ₃ Ti	Pt ₃ V	Pt ₃ Cr	Pt ₃ Mn	Pt ₃ Fe	Pt ₃ Co	Pt ₃ Ni
Bader Charge	C ₁	+0.72	+0.78	+0.93	+0.70	+0.71	+0.68	+0.73	+0.62	+0.75
	C ₂	+0.65	+0.73	+0.32	+0.67	+0.57	+0.58	+0.60	−0.20	−0.22
	O	−1.61	−1.63	−1.42	−1.65	−1.64	−1.64	−1.65	−1.64	−1.61
	Pt ₁	−0.16	−0.59	−0.84	−0.61	−0.51	−0.49	−0.44	−0.39	−0.35
	Pt ₂	+0.25	−0.1	+0.04	−0.13	−0.02	−0.03	+0.01	+0.06	+0.09
	Pt ₃	+0.19	−0.11	−0.52	−0.09	−0.07	−0.04	+0.01	+0.08	+0.11
	M(or Pt ₀)	−0.12	+1.56	+2.13	+1.70	+1.28	+1.12	+0.97	+0.71	+0.57
d _(O-OG) /Å		0.17	0.51	0.60	0.57	0.42	0.38	0.40	0.20	0.18

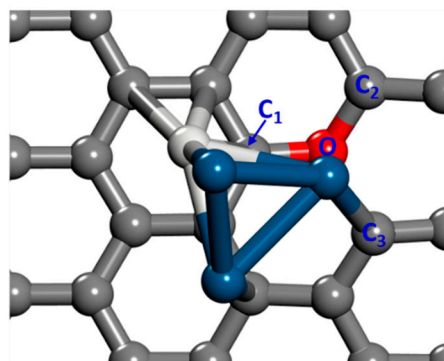
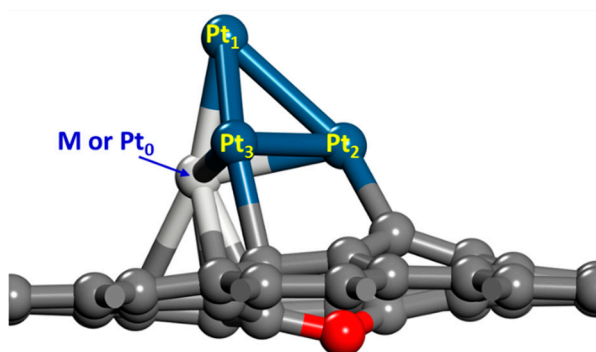


Table 1 lists the Bader charges of C₁, C₂, O, Pt₁, Pt₂, Pt₃, and M (or Pt₀) in the optimized Pt₃M on OG, with numbering of the atoms shown in the figures under Table 1. The charges of the doped O atom and the two linking C atoms were generally maintained at similar values for different Pt₃M clusters. The exception was the C₂ atom in Pt₃Co and Pt₃Ni due to the O–C₂ bond breaking and the O–C₃ bond formation. In supported Pt₄, two Pt atoms were positively charged, whereas the other two were negatively charged, although the charge differences were not great. When a second metal was introduced to replace one of the Pt atoms to form Pt₃M, charge localization occurred. In particular, the top Pt₁ atom was significantly more negatively charged, whereas the M atom was positively charged and the charge on M decreased from 2.13 |e| on Ti to 0.57 |e| on Ni, due mainly to the change of the electronic structure and atomic radius. We note that the charge on the more active early transition metals (M for M = Sc, Ti, V, and Cr) was much larger than those on the late transition metals (M = Mn, Fe, Co, and Ni). These differences in charge redistribution will in turn affect the oxygen adsorption energies and ORR reactivity.

To characterize the stability of supported Pt₃M on OG, we defined a net binding energy (E_b) as $\Delta E_b = E_b(\text{Pt}_4) - E_b(\text{Pt}_3\text{M})$, i.e., the binding energy difference of OG–Pt₃M and OG–Pt₄, and plotted the results in Figure 1. According to this definition, a positive value would indicate that the Pt₃M cluster binds OG stronger than Pt₄. As shown in Figure 1, the binding energy of Pt₃Mn and Pt₃Fe was closer to Pt₄, while the binding energy difference was highly negative for Pt₃Ti and Pt₃V, indicating that these two clusters bind OG much weaker than Pt₄. On the other hand, Pt₃M with M = Sc, Cr, Co, and Ni binds OG more strongly than Pt₄, by ~0.1 eV, indicating their higher stabilities. The relative stability of OG–Pt₃M is a reflection of the interaction between Pt₃M and support and will affect the ORR performance.

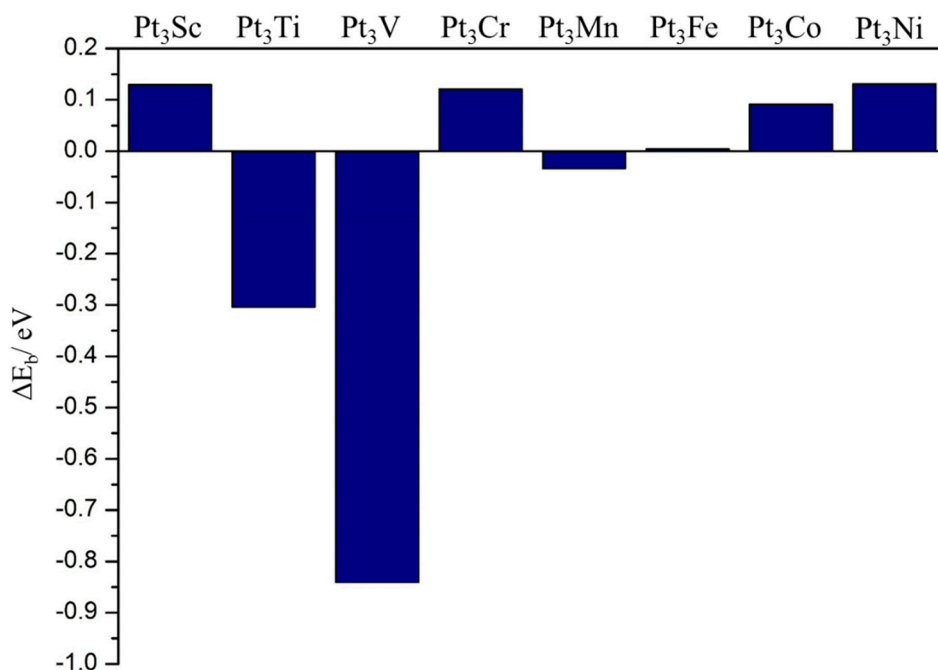


Figure 1. Net binding energy of Pt₃M on O-doped graphene (OG) with respect to Pt₄ on OG.

2.2. Oxygen Adsorption and Reduction Mechanism

The mechanism of ORR on various electrocatalysts was extensively investigated using the density functional theory (DFT) method [4,27,39–42]. Previously, we studied the ORR mechanism over the OG supported Pt₄, Pt₃V, and Pt₃Fe clusters and reported two possible pathways [36]. Herein, we expanded the investigation to include all 3d transition metals.

The first step for oxygen reduction is O₂ adsorption. We calculated the possible adsorption structures of O₂ on OG–Pt₃M and found that O₂ prefers to bind the supported cluster in a di-oxygen form in a bridging configuration, with one oxygen atom on Pt₁ and another on M, as can be seen in Figure 2 and Figure S1. The O–O distance of these adsorbed di-oxygen species was stretched to 1.41~1.47 Å from 1.23 Å of the isolated O₂ molecule. Interestingly, the Pt₃M cluster maintained a tetrahedral structure after being combined with O₂, in contrast to Pt₄, which was transformed into a planar-ring structure by O₂ adsorption, indicating that the transition metal atoms in Pt-based alloys contribute to stabilizing the cluster structure.

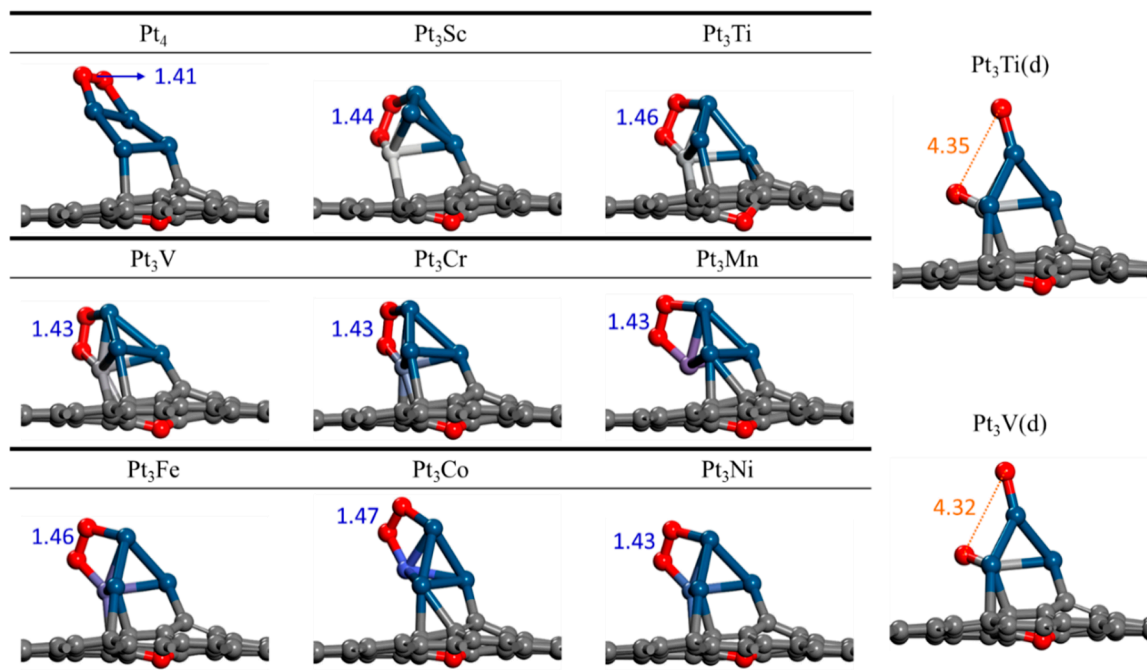


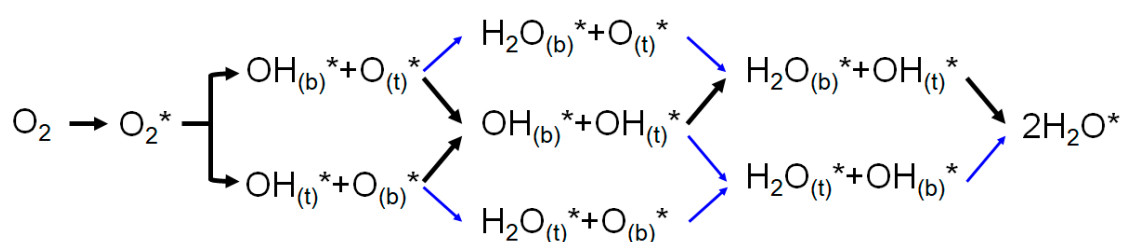
Figure 2. Adsorption configuration and O–O bond distance (shown in Å) of O₂ on OG–Pt₃M. The left three columns show O₂ adsorbed as di-oxygen species, while the two structures on the right are the O adatoms on supported Pt₃Ti and Pt₃V. Red, dark blue, and grey spheres represent O, Pt, and C, respectively. The color of M is different and depends on the element.

In addition to the di-oxygen form of adsorption, dissociative adsorption of O₂ occurred on OG–Pt₃Ti and OG–Pt₃V, resulting in two O adatoms with O–O distances of 4.35 Å and 4.32 Å, respectively (shown in Figure 2). The dissociative adsorption was more stable than the di-oxygen state, by 1.61 eV for Pt₃Ti and 2.65 eV for Pt₃V. Based on Bader charge analysis, the Ti and V atoms in clusters had the highest positive charges among the 3d transition metals, with values of 2.13 |e| and 1.70 |e|, respectively. The oxygen atoms bound to the Ti and V atoms were more negatively charged than the oxygen adatom on Pt₁, indicating that the oxygen atoms in the adsorbed di-oxygen state were strongly polarized by the large difference of electron distribution between Ti/V and Pt₁. As a result, the dissociative adsorption of oxygen was more stable than the di-oxygen state on Pt₃Ti and Pt₃V, which also hindered the following H₂O formation and release. In contrast, the charge difference between the two adsorbed oxygen atoms in the di-oxygen form on other Pt₃M clusters fell in a small range of 0.07~0.17 |e|, and consequently, the adsorbed di-oxygen species was more stable. In order to compare the ORR activity on these supported Pt₃M, we chose the di-oxygen species as the reference.

The reduction of adsorbed di-oxygen species occurs by adding a hydrogen atom either on the top O atom on Pt₁ or the interfacial O atom on M. On Pt(111), ORR was believed to proceed via the OOH* intermediate [39,40,43]. However, a stable OOH* intermediate was not isolated on any of the OG–Pt₃M catalysts. Upon hydrogenation, the di-oxygen species dissociates into co-adsorbed O* and OH* species on all Pt₃M. For the early transition metals (M = Ti, V, and Cr), protonation of the top O of

the di-oxygen species leads to more stable $\text{OH}_{(t)}^*$ and O^* , while for the late transition metals ($M = \text{Mn}, \text{Fe}, \text{Co}, \text{and Ni}$), the formation of $\text{OH}_{(b)}^*$ with the interfacial O atom and leaving the top O as O^* is more stable (suffix “t” and “b” correspond to the species on the top Pt_1 atom and the interfacial M (or Pt_0) atom, respectively).

Further reduction after either $\text{OH}_{(t)}^*$ or $\text{OH}_{(b)}^*$ formation may follow two pathways, as shown in Scheme 1. The calculated reaction free energy for every elementary step indicates that protonating two O^* s to form two OH^* s is more preferable than hydrogenating one O^* completely to H_2O^* before hydrogenating the other O^* . Further reducing the OH^* species will produce H_2O^* , which will desorb and liberate the active sites for the continued O_2 adsorption and reduction (see Tables S2 and S3 for details). The step with the most positive reaction free energy is the hydrogenation of the OH^* species, which is likely to be the potential-limiting step. Between $\text{OH}_{(t)}^*$ and $\text{OH}_{(b)}^*$, the reduction of $\text{OH}_{(b)}^*$ has a lower reaction free energy and is more favorable than reducing the $\text{OH}_{(t)}^*$. In Scheme 1, the most favorable pathway is shown in bold black.



Scheme 1. Reaction pathways of the oxygen reduction reaction (ORR). Labels “b” or “t” correspond to the species on the interfacial M (or Pt_0) atom or the top Pt_1 atom. The pathway following the bold black arrows is the thermodynamically more favorable one.

To compare the reaction on different OG- Pt_3M catalysts, the free energy profiles for ORR through the interfacial site at 0 and 0.85 V (SHE) were constructed on the basis of the DFT results (see details in Figures S2 and S3). Compared with the results on OG- Pt_4 , the adsorption of O_2 was strengthened on Pt_3M with $M = \text{Sc}, \text{Ti}, \text{V}, \text{and Cr}$. On Pt_3M with $M = \text{Mn}, \text{Fe}, \text{Co}, \text{and Ni}$, the O_2 adsorption energy became 0.1–0.4 eV smaller than that on Pt_4 . These results are consistent with previous studies [37,44]. Figure 3 shows a comparison of the free energy profiles of ORR on OG- Pt_4 , OG- Pt_3Ti , and OG- Pt_3Ni . Obviously, oxygen bound much stronger on Pt_3Ti than on Pt_4 : the binding energy on the supported Pt_3Ti was increased by 0.71 eV, resulting in a highly stable OH^* species, which is difficult to hydrogenate to H_2O . In the case of Pt_3Ni , the adsorption energy of oxygen was decreased by 0.4 eV from that of Pt_4 . By applying a potential of 0.85 V (SHE), the reduction of OH^* to form H_2O^* on Pt_3Ni became less endothermic than Pt_4 . In addition, the desorption of H_2O^* became easier than that on Pt_4 , indicating an enhanced ORR activity on Pt_3Ni .

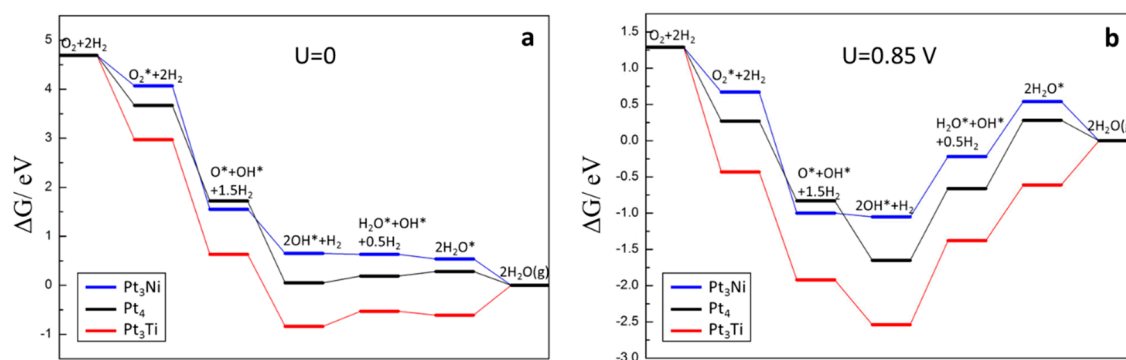


Figure 3. Free energy profiles of ORR on OG-supported Pt_4 (black line), Pt_3Ti (red line), and Pt_3Ni (blue line) clusters at 0 V (a) and 0.85 V (b) with respect to the standard hydrogen electrode (SHE).

2.3. Correlation of the ORR Activity with the Oxygen Binding Energy Difference

To design an electrocatalyst with improved ORR activity, understanding the relationship between the activity and atomic/electronic structures of the catalyst is important [1,37,45]. On transition metal- and/or metal alloy-based catalysts, the linear relationship between the ORR activity and the d-band center of those electrocatalysts has been established [13,20,37,46,47]. The oxygen binding energy (ΔE_O) has been used as a descriptor for the ORR activity on the transition metal and even on non-metallic surfaces [1,39,48,49]. In fact, the ΔE_O descriptor can be considered an extension and application of the d-band center model in electrocatalysis, as the adsorption/binding energy of oxygen has been shown to correlate with the d states of the surface atoms to which the atom/molecule binds [13,37]. Generally, an upward shift of the d-band center to Fermi level results in a stronger binding [13,17,24]. However, both the d-band center model and the oxygen-binding energy descriptor have limitations [14,50,51]. For example, Lin et al. reported that the ORR activity of the Pt-cored alloy (Pt@M, M = Co, Cu, Pd, and Au) catalysts does not correlate well with the d-band center of surface Pt [17]. Yu et al. showed that the binding energies of O do not always correlate with those of OH [52].

To understand the performance difference of the Pt₃M alloy catalysts in the present study, we plotted the average adsorption energy of di-oxygen species ($1/2 \Delta E_{O_2}$) on the OG-Pt₃M as a function of the d-band center (ϵ_d) of the cluster atoms (as shown in Figure S4) and found a very weak linear correlation. In fact, the present results indicate that a higher d-band center in the clusters involving late transition metals (M = Mn, Fe, Co, and Ni) corresponds to a lower oxygen adsorption energy. Previous reports showed that the adsorption energy of O* had a strong correlation with the adsorption energy of OH* [53–55]. Herein, we evaluated the possible correlation between the adsorption energies of O* and OH* on the interfacial sites of the supported Pt₃M (seen in Figure S5) and also found a rather weak linear correlation, demonstrating that neither ΔE_O nor ϵ_d is a good descriptor of the ORR activity of the OG-Pt₃M.

Charge redistribution is expected to occur upon formation of the O* and OH* species. We analyzed the Bader charge of the interfacial M sites ($q(M)$) upon forming the O* and OH* adsorbates, as well as the those of the OH* and O* ($q(O)$) on different alloy clusters. As shown in Figure 4a, there was quite a good linear correlation between $q(M)$ and the charges on OH_b* and O_b*. The slope of the lines is ~1.06, indicating a similar electron transfer from M to OH_b* and O_b*. In the 3d transition metal series, the late transition metals (including Ni, Co, Fe, and Mn) transferred fewer electronic charges to the adsorbates than the early transition metals and resulted in a relatively weaker binding of O*.

From Figure 4b, the positive charges on the interfacial M site generally increased by following the order of the 3d elements in the periodic table from right to left, with the exception of Sc upon O* formation. In OG-Pt₃Sc, the positive charge on Sc with adsorbed O_b* was even smaller than that on Cr in Pt₃Cr. We also plotted the adsorption energy of O_b* ($\Delta E(O_b)$) against $q(M)$ of O_b* (seen in Figure S6) and found no strong correlation between the two.

Since the O₂ molecule prefers to form a di-oxygen species on the bridge sites of the top Pt₁ and interfacial M (or Pt₀) atoms, both sites were expected to contribute to the ORR activity. Therefore, we needed a descriptor that takes into the contribution of both sites to account for the observed ORR activity. Herein, we used the adsorption energy difference between the interfacial oxygen adatom O_b* and the top oxygen adatom O_t* species ($\Delta E_{O_b-O_t}$) to characterize the clusters and plotted the adsorption energy difference on each OG-Pt₃M as a function of $q(M)$ of O_b* in Figure 4c. As shown in the figure, there was a reasonable correlation between the two ($R^2 = 0.64$). The correlations shown in Figure 4 are useful to understand the observed ORR activity, although they cannot be used as a descriptor to predict superior ORR catalysts.

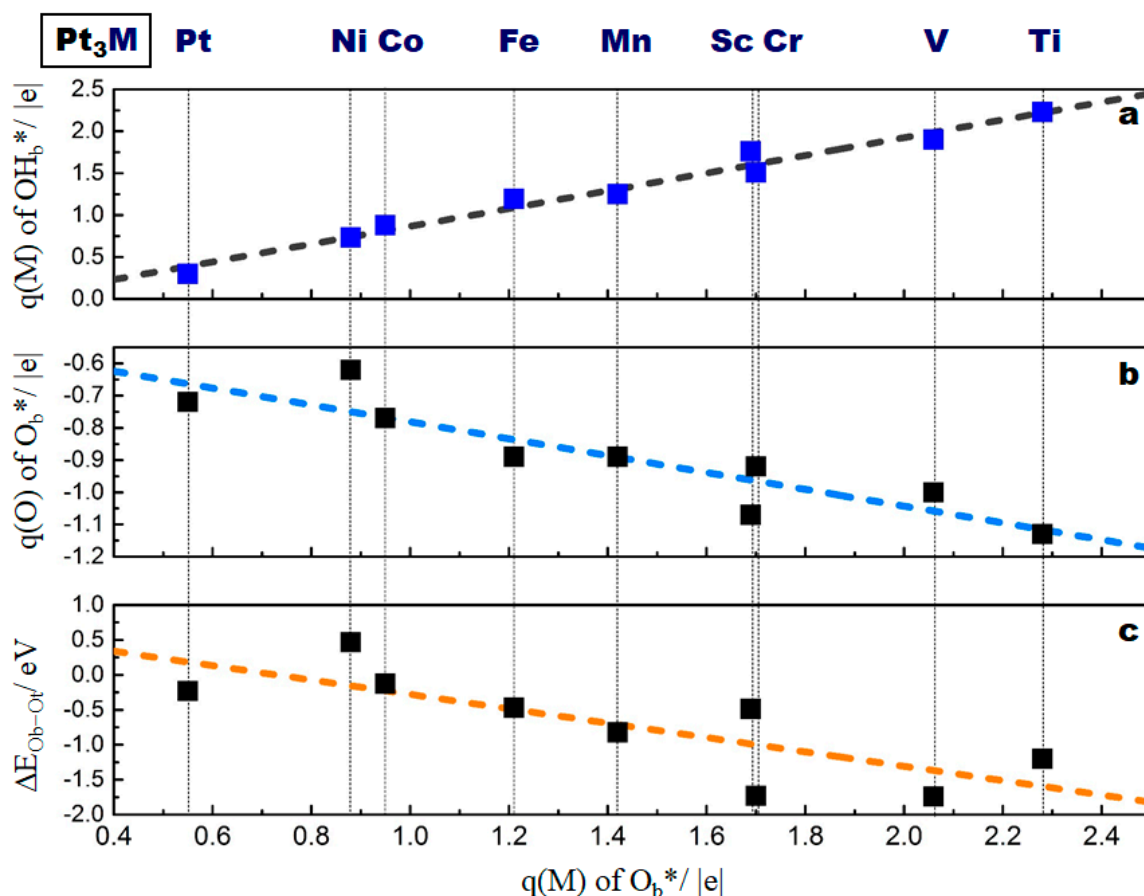


Figure 4. The Bader charges on the (a) OH* intermediate, (b) O_b* adatoms, and (c) the adsorption energy difference between O_b* and O_t* as a function of the charge changes of interfacial M sites. The vertical dash line indicates the location of the Bader charge values of the corresponding element.

Both the O* and OH* species are important intermediates for ORR, and their stability will have a strong influence on the overall reaction activity. However, the adsorption energy of individual OH* and O* only shows a weak linear relationship on the single interfacial site. As the adsorption energy difference of ΔE_{Ob-Ot} presents a good correlation with the charge changes of cluster, we investigated the adsorption energy difference of OH* species adsorbed on the interfacial and top sites ($\Delta E_{OHb-OHt}$). The correlation between $\Delta E_{OHb-OHt}$ and ΔE_{Ob-Ot} is shown in Figure 5a. Following the increased energy difference of O*, O* adsorbed on the interfacial site became less stable, resulting in a similar trend to that of the OH* species. Compared to pure Pt₄, Pt₃Ni and Pt₃Co showed weaker binding toward the O* and OH* at the interfacial M site. All the other Pt₃M_s exhibited stronger binding toward O* at the interfacial M site. Therefore, the adsorption energy difference between the top Pt site and the interfacial M site provides a good indicator of the alloying effect on the ORR reactivity.

In Figure 5b, the reaction free energy of the potential limiting step was plotted as a function of the adsorption energy difference of O* on top and interfacial sites. Again, a good correlation ($R^2 = 0.81$) was obtained. In general, a higher positive adsorption energy difference corresponds to a lower reaction-free energy, and therefore, a higher activity. If the OG–Pt₄ is chosen as a reference, both Pt₃Fe and Pt₃Ni have smaller reaction free energies, indicating a better ORR performance than Pt₄. Among all the OG–Pt₃M_s, Ni exhibited the largest decrease in the reaction free energy, and thereby, the limiting potential. Consequently, OG–Pt₃Ni is the best catalyst among all OG–Pt₃M_s. This conclusion is supported by the free energy profiles (Figures S2 and S3). The limiting potential for ORR on OG–Pt₃Ni was reduced to 0.83 V from 1.00 V on OG–Pt₄.

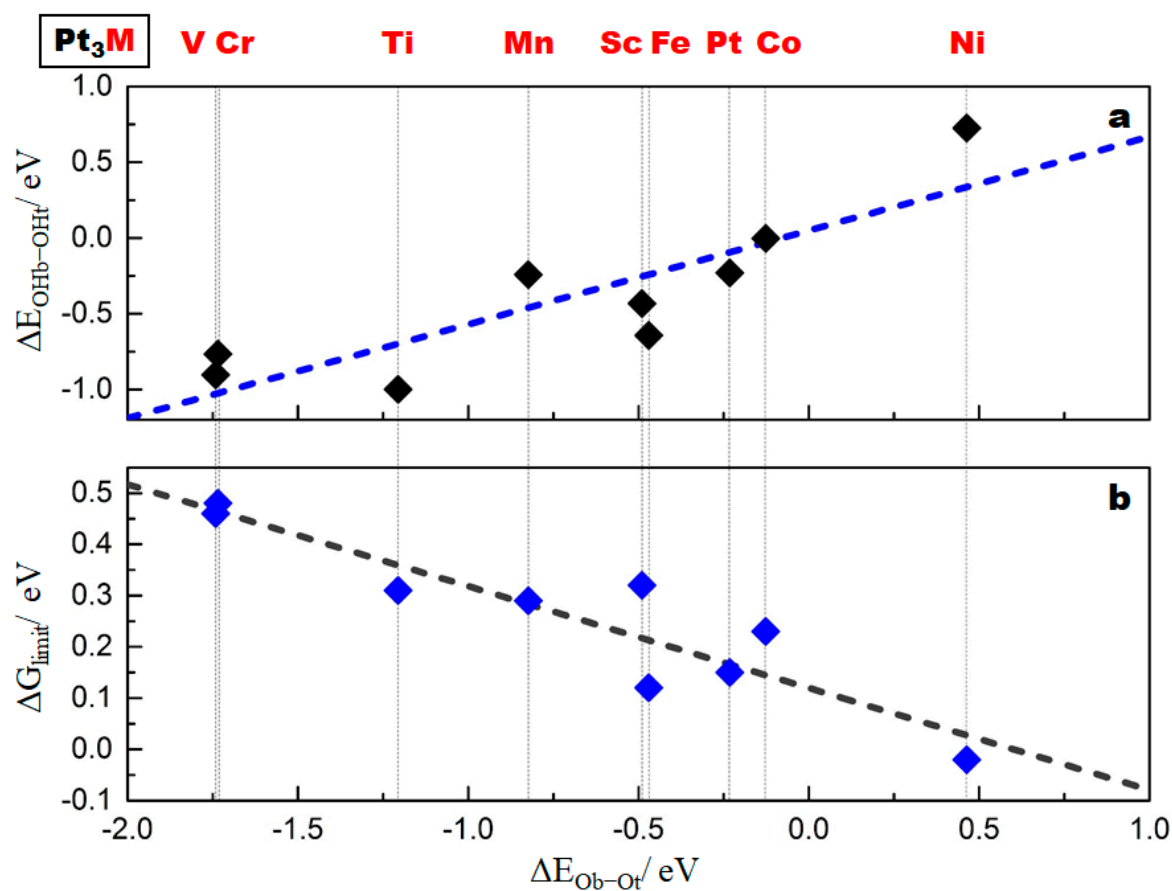


Figure 5. The correlations of (a) the adsorption energy difference between OH* species adsorbed on the interfacial and top sites ($\Delta E_{\text{OHb-OHt}}$), and (b) the free energy change for the rate limiting step (ΔG_{limit}) of ORR to the oxygen adsorption energy difference of both sites ($\Delta E_{\text{Ob-Ot}}$).

The present analysis demonstrated that oxygen adsorption energy alone is not effective in predicting ORR reactivity. For the alloy catalysts, the adsorption of the ORR intermediates on different metal sites should be taken into account when both metals participate in the reaction. On the OG-Pt₃M catalysts, $\Delta E_{\text{Ob-Ot}}$ provides a more effective indicator of the ORR activity. In reactions involving sites of different metals, the adsorption energy difference between the alloying metals would provide a more complete description of the ORR activity.

3. Model and Computational Details

Spin unrestricted DFT calculations were performed using the Vienna ab initio simulations program (VASP), with the projector augmented wave method [56–58]. In short, the Perdew–Burke–Ernzerhof functional [59] and a cutoff energy of 400 eV for the plane wave basis set were used in the calculations. The same oxygen-doped graphene supercell of $12.30 \times 17.04 \text{ \AA}$ with a vacuum of 20 Å as that used in our previous work was employed in the present study [36], and the same $3 \times 2 \times 1$ k-point grid and convergence criteria were used in the present study.

The binding energy (E_b) of metal clusters (Pt₃M) on the OG support was calculated as $E_b = E_{\text{OG-Pt3M}} - (E_{\text{OG}} + E_{\text{Pt3M}})$, with $E_{\text{OG-Pt3M}}$, E_{OG} , and E_{Pt3M} being the total energies of the OG with supported metal cluster, isolated OG sheet, and metal cluster, respectively. The adsorption energies of O₂ on the supported metal clusters were calculated with respect to the gas-phase O₂ molecules. The Gibbs free energy change (ΔG) of the elementary reactions was used to identify the most favorable oxygen reduction reaction pathway. The free energies of every intermediate along the reaction pathways were calculated based on the computational hydrogen electrode (CHE) model proposed by Nørskov

et al. [53,60,61]. The reference potential was set to the standard hydrogen electrode (SHE), i.e., the free energy of ($\text{H}^+ + \text{e}^-$) equaled half of the chemical potential of a gas-phase H_2 at 0 V under the standard conditions of $\text{pH} = 0$ and the pressure of H_2 was 1 bar. The free energy change for each elementary step was determined as $\Delta G = \Delta E + \Delta \text{ZPE} - T\Delta S + \Delta G_U$, where ΔE corresponds to the reaction energy calculated using DFT. ΔZPE and $-T\Delta S$ are the corrections due to zero-point energy (ZPE) and entropy (S) at 300 K. Both ZPE and S were calculated based on the harmonic vibrational frequencies. Adding $\Delta G_U = -eU$, where e is the unit positive charge and U is the electrode potential with respect to SHE, will allow the external potential to modulate the chemical potential change of an elementary step. The entropic contribution of gas-phase molecules was taken from the National Institute of Standards and Technology database [62].

Bader charge analysis was conducted for every OG-supported Pt_3M (OG- Pt_3M) catalyst [63,64]. The d-band centers (ϵ_d) of Pt atoms in the cluster were calculated based on the follow equation:

$$\epsilon_d = \frac{\int_{-\infty}^{\epsilon_F} \rho \cdot E \, d\epsilon}{\int_{-\infty}^{\epsilon_F} \rho \, d\epsilon}$$

in which ρ , E , and ϵ_F represent the density of electronic states, the energy of electron, and Fermi energy, respectively [50,65]. The reaction free energy of an elementary step refers to the Gibbs free energy difference of reactant and product. The kinetic barrier originating from the non-electrochemical activation of the reactant was not considered in the present study. The barriers associated with the electron and proton transfer were believed to be small and were also not considered in the present study [66].

4. Conclusions

We performed a DFT computational study on the mechanism and activity of O-doped graphene-supported Pt_4 and Pt_3M ($\text{M} = \text{Sc}, \text{Ti}, \text{V}, \text{Cr}, \text{Mn}, \text{Fe}, \text{Co},$ and Ni) catalysts toward oxygen reduction reactions. Co-adsorbed H_2O^* and O^* species are highly unlikely and water formation is the potential limiting step on the supported Pt_3M catalysts.

The late transition metal alloyed clusters ($\text{M} = \text{Mn}, \text{Fe}, \text{Co},$ and Ni), especially Pt_3Co and Pt_3Ni , bound the oxygen intermediates weaker than Pt_4 and would have a better ORR activity. On the other hand, alloying with an early transition metal atom ($\text{M} = \text{Sc}, \text{Ti}, \text{V},$ and Cr) increased the binding energy of the oxygen intermediates, thereby hindering the oxygen reduction process. Among the systems examined, OG- Pt_3Ni lowered the adsorption energies of O and OH the most and was the best catalyst for ORR. The present study demonstrated that the oxygen adsorption energy alone may not be a good predictor of the ORR activity. Instead, the oxygen adsorption energy difference on the ensemble of the active sites ($\Delta E_{\text{O}_b-\text{O}_t}$) is an effective indicator of the ORR activity.

Supplementary Materials: The following are available online at <http://www.mdpi.com/2073-4344/10/2/156/s1>, Table S1: Optimized structures for every O-doped graphene (OG) supported Pt_3M ($\text{M} = 3\text{d}$ transition metals) and Pt_4 alloy clusters. Table S2. Free energy change (ΔG) of every elementary step of ORR for different OG supported Pt_3M and Pt_4 clusters as the interfacial site is first hydrogenated. Table S3. Free energy change (ΔG) of every elementary step of ORR for different OG supported Pt_3M and Pt_4 clusters as the top site is first hydrogenated. Figure S1. End-on adsorption of O_2 on the bottom M atom of OG- Pt_3M and the corresponding relative adsorption energy with respect to bridging di-oxygen form. Figure S2. Free energy diagrams for oxygen reduction on OG supported Pt_3M ($\text{M} = 3\text{d}$ transition metals) and Pt_4 clusters at 0 V. Figure S3. Free energy diagrams for oxygen reduction on OG supported Pt_3M ($\text{M} = 3\text{d}$ transition metals) and Pt_4 clusters at 0.85 V (SHE). Figure S4. Average adsorption energies of O_2 on the OG- Pt_3M clusters as a function of the d-band center (ϵ_d) of the Pt atoms in clusters. **Figure S5.** Relationship between the adsorption energy of O^* and OH^* on the interfacial sites of Pt_3M alloy clusters. **Figure S6.** The adsorption energy of oxygen atom on the bottom site ($\Delta E(\text{O}_b)$) as a function of the Bader charge $q(\text{M})$ of O_b^* intermediate.

Author Contributions: C.C. and M.S. performed the calculations and drafted the manuscript; X.Z. and J.H. helped to collect and analyze the data; H.W. and Q.G. revised the manuscript. All authors have read and agreed to the published version of the manuscript.

Funding: This research was funded by National Natural Sciences Foundation of China (Grant No.21576204, 21206117, and 21373148).

Acknowledgments: The High Performance Computing Center of Tianjin University is acknowledged for providing services to computing resources.

Conflicts of Interest: The authors declare no conflict of interest.

References

1. Zagal, J.H.; Koper, M.T.M. Reactivity Descriptors for the Activity of Molecular MN₄ Catalysts for the Oxygen Reduction Reaction. *Angewandte Chemie Int. Ed.* **2016**, *55*, 14510–14521. [\[CrossRef\]](#) [\[PubMed\]](#)
2. Zhong, X.; Yu, H.; Wang, X.; Liu, L.; Jiang, Y.; Wang, L.; Zhuang, G.; Chu, Y.; Li, X.; Wang, J.-G. Pt@Au Nanorods Uniformly Decorated on Pyridyne Cycloaddition Graphene as a Highly Effective Electrocatalyst for Oxygen Reduction. *ACS Appl. Mater. Interfaces* **2014**, *6*, 13448–13454. [\[CrossRef\]](#) [\[PubMed\]](#)
3. Kumar, A.; Zhang, Y.; Liu, W.; Sun, X. The chemistry, recent advancements and activity descriptors for macrocycles based electrocatalysts in oxygen reduction reaction. *Coord. Chem. Rev.* **2020**, *402*, 213047. [\[CrossRef\]](#)
4. Sha, Y.; Yu, T.H.; Merinov, B.V.; Goddard, W.A., III. DFT Prediction of Oxygen Reduction Reaction on Palladium-Copper Alloy Surfaces. *ACS Catal.* **2014**, *4*, 1189–1197. [\[CrossRef\]](#)
5. Antolini, E. Effect of Structural Characteristics of Binary Palladium-Cobalt Fuel Cell Catalysts on the Activity for Oxygen Reduction. *ChemPlusChem* **2014**, *79*, 765–775. [\[CrossRef\]](#)
6. Wu, P.; Du, P.; Zhang, H.; Cai, C. Graphyne As a Promising Metal-Free Electrocatalyst for Oxygen Reduction Reactions in Acidic Fuel Cells: A DFT Study. *J. Phys. Chem. C* **2012**, *116*, 20472–20479. [\[CrossRef\]](#)
7. Hyun, K.; Lee, J.H.; Yoon, C.W.; Kwon, Y. The Effect of Platinum Based Bimetallic Electrocatalysts on Oxygen Reduction Reaction of Proton Exchange Membrane Fuel Cells. *Int. J. Electrochem. Sci.* **2013**, *8*, 11752–11767.
8. Zhang, B.-W.; Zhang, Z.-C.; Liao, H.-G.; Gong, Y.; Gu, L.; Qu, X.-M.; You, L.-X.; Liu, S.; Huang, L.; Tian, X.-C.; et al. Tuning Pt-skin to Ni-rich surface of Pt₃Ni catalysts supported on porous carbon for enhanced oxygen reduction reaction and formic electro-oxidation. *Nano Energy* **2016**, *19*, 198–209. [\[CrossRef\]](#)
9. Stephens, I.E.L.; Bondarenko, A.S.; Perez-Alonso, F.J.; Calle-Vallejo, F.; Bech, L.; Johansson, T.P.; Jepsen, A.K.; Frydendal, R.; Knudsen, B.P.; Rossmeisl, J.; et al. Tuning the Activity of Pt (111) for Oxygen Electroreduction by Subsurface Alloying. *J. Am. Chem. Soc.* **2011**, *133*, 5485–5491. [\[CrossRef\]](#)
10. Deng, K.; Xu, Y.; Li, Y.; Dai, Z.; Wang, Z.; Li, X.; Wang, H.; Wang, L. Integration mesoporous surface and hollow cavity into PtPdRh nano-octahedra for enhanced oxygen reduction electrocatalysis. *Nanotechnology* **2020**, *31*, 025401. [\[CrossRef\]](#)
11. Zhao, Z.; Chen, C.; Liu, Z.; Huang, J.; Wu, M.; Liu, H.; Li, Y.; Huang, Y. Pt-Based Nanocrystal for Electrocatalytic Oxygen Reduction. *Adv. Mater.* **2019**, *31*, 1808115. [\[CrossRef\]](#) [\[PubMed\]](#)
12. Wu, Z.; Dang, D.; Tian, X. Designing Robust Support for Pt Alloy Nanoframes with Durable Oxygen Reduction Reaction Activity. *ACS Appl. Mater. Interfaces* **2019**, *11*, 9117–9124. [\[CrossRef\]](#) [\[PubMed\]](#)
13. Stamenkovic, V.R.; Mun, B.S.; Arenz, M.; Mayrhofer, K.J.J.; Lucas, C.A.; Wang, G.; Ross, P.N.; Markovic, N.M. Trends in electrocatalysis on extended and nanoscale Pt-bimetallic alloy surfaces. *Nat. Mater.* **2007**, *6*, 241–247. [\[CrossRef\]](#)
14. Cheng, D.; Qiu, X.; Yu, H. Enhancing oxygen reduction reaction activity of Pt-shelled catalysts via subsurface alloying. *Phys. Chem. Chem. Phys.* **2014**, *16*, 20377–20381. [\[CrossRef\]](#)
15. Nguyen, M.T.; Wakabayashi, R.H.; Yang, M.; Abruna, H.D.; DiSalvo, F.J. Synthesis of carbon supported ordered tetragonal pseudo-ternary Pt₂M'M'' (M = Fe, Co, Ni) nanoparticles and their activity for oxygen reduction reaction. *J. Power Sources* **2015**, *280*, 459–466. [\[CrossRef\]](#)
16. Wang, Q.; Tao, H.; Li, Z.; Wang, G. Effect of iron precursor on the activity and stability of PtFe/C catalyst for oxygen reduction reaction. *J. Alloys Compd.* **2020**, *814*, 152212. [\[CrossRef\]](#)
17. Lin, S.-P.; Wang, K.-W.; Liu, C.-W.; Chen, H.-S.; Wang, J.-H. Trends of Oxygen Reduction Reaction on Platinum Alloys: A Computational and Experimental Study. *J. Phys. Chem. C* **2015**, *119*, 15224–15231. [\[CrossRef\]](#)
18. Zhang, L.; Fischer, J.M.T.A.; Jia, Y.; Yan, X.; Xu, W.; Wang, X.; Chen, J.; Yang, D.; Liu, H.; Zhuang, L.; et al. Coordination of Atomic Co-Pt Coupling Species at Carbon Defects as Active Sites for Oxygen Reduction Reaction. *J. Am. Chem. Soc.* **2018**, *140*, 10757–10763. [\[CrossRef\]](#)

19. Tian, X.; Zhao, X.; Su, Y.-Q.; Wang, L.; Wang, H.; Dang, D.; Chi, B.; Liu, H.; Hensen, E.J.M.; Lou, X.W.; et al. Engineering bunched Pt-Ni alloy nanocages for efficient oxygen reduction in practical fuel cells. *Science* **2019**, *366*, 850–856. [\[CrossRef\]](#)
20. Ou, L. The origin of enhanced electrocatalytic activity of Pt-M (M = Fe, Co, Ni, Cu, and W) alloys in PEM fuel cell cathodes: A DFT computational study. *Comput. Theor. Chem.* **2014**, *1048*, 69–76. [\[CrossRef\]](#)
21. Gatalo, M.; Moriau, L.; Petek, U.; Ruiz-Zepeda, F.; Sala, M.; Grom, M.; Galun, T.; Jovanovic, P.; Pavlisic, A.; Bele, M.; et al. CO-assisted ex-situ chemical activation of Pt-Cu/C oxygen reduction reaction electrocatalyst. *Electrochim. Acta* **2019**, *306*, 377–386. [\[CrossRef\]](#)
22. Zhu, C.; Dong, S. Recent progress in graphene-based nanomaterials as advanced electrocatalysts towards oxygen reduction reaction. *Nanoscale* **2013**, *5*, 1753–1767. [\[CrossRef\]](#) [\[PubMed\]](#)
23. Higgins, D.; Zamani, P.; Yu, A.; Chen, Z. The application of graphene and its composites in oxygen reduction electrocatalysis: A perspective and review of recent progress. *Energy Environ. Sci.* **2016**, *9*, 357–390. [\[CrossRef\]](#)
24. Chen, H.S.; Liang, Y.T.; Chen, T.Y.; Tseng, Y.C.; Liu, C.W.; Chung, S.R.; Hsieh, C.T.; Lee, C.E.; Wang, K.W. Graphene-supported Pt and PtPd nanorods with enhanced electrocatalytic performance for the oxygen reduction reaction. *Chem. Commun.* **2014**, *50*, 11165–11168. [\[CrossRef\]](#)
25. Yan, Z.H.; Wang, M.; Huang, B.X.; Liu, R.M.; Zhao, J.S. Graphene Supported Pt-Co Alloy Nanoparticles as Cathode Catalyst for Microbial Fuel Cells. *Int. J. Electrochem. Sci.* **2013**, *8*, 149–158.
26. Boone, C.V.; Maia, G. Lowering metal loadings onto Pt-Pd-Cu/graphene nanoribbon nanocomposites affects electrode collection efficiency and oxygen reduction reaction performance. *Electrochim. Acta* **2019**, *303*, 192–203. [\[CrossRef\]](#)
27. Fazio, G.; Ferrighi, L.; Di Valentin, C. Boron-doped graphene as active electrocatalyst for oxygen reduction reaction at a fuel-cell cathode. *J. Catal.* **2014**, *318*, 203–210. [\[CrossRef\]](#)
28. Wang, S.Y.; Zhang, L.P.; Xia, Z.H.; Roy, A.; Chang, D.W.; Baek, J.B.; Dai, L.M. BCN Graphene as Efficient Metal-Free Electrocatalyst for the Oxygen Reduction Reaction. *Angewandte Chemie Int. Ed.* **2012**, *51*, 4209–4212. [\[CrossRef\]](#)
29. Zhang, L.P.; Xia, Z.H. Mechanisms of Oxygen Reduction Reaction on Nitrogen-Doped Graphene for Fuel Cells. *J. Phys. Chem. C* **2011**, *115*, 11170–11176. [\[CrossRef\]](#)
30. del Cueto, M.; Ocon, P.; Poyato, J.M.L. Comparative Study of Oxygen Reduction Reaction Mechanism on Nitrogen-, Phosphorus-, and Boron-Doped Graphene Surfaces for Fuel Cell Applications. *J. Phys. Chem. C* **2015**, *119*, 2004–2009. [\[CrossRef\]](#)
31. Shi, X.; Zhang, J.; Huang, T. Significant advantages of sulfur-doped graphene in neutral media as electrocatalyst for oxygen reduction comparing with Pt/C. *IOP Conf. Ser. Earth Environ. Sci.* **2018**, *121*, 022011. [\[CrossRef\]](#)
32. Cui, H.; Zhou, Z.; Jia, D. Heteroatom-Doped Graphene as Electrocatalysts for Air Cathodes. *Mater. Horiz.* **2017**, *4*, 7–19. [\[CrossRef\]](#)
33. Xu, J.; Wang, Y.; Hu, S. Nanocomposites of graphene and graphene oxides: Synthesis, molecular functionalization and application in electrochemical sensors and biosensors. A review. *Microchim. Acta* **2017**, *184*, 1–44. [\[CrossRef\]](#)
34. Su, C.; Loh, K.P. Carbocatalysts: Graphene Oxide and Its Derivatives. *Acc. Chem. Res.* **2013**, *46*, 2275–2285. [\[CrossRef\]](#)
35. Tang, Y.; Chen, T.; Guo, W. Surfactant-Free Synthesis of Reduced Graphene Oxide Supported Well-Defined Polyhedral Pd-Pt Nanocrystals for Oxygen Reduction Reaction. *Catalysts* **2019**, *9*, 756. [\[CrossRef\]](#)
36. Jin, N.; Han, J.; Wang, H.; Zhu, X.; Ge, Q. A DFT study of oxygen reduction reaction mechanism over O-doped graphene-supported Pt-4, Pt3Fe and Pt3V alloy catalysts. *Int. J. Hydrogen Energy* **2015**, *40*, 5126–5134. [\[CrossRef\]](#)
37. Stamenkovic, V.; Mun, B.S.; Mayrhofer, K.J.J.; Ross, P.N.; Markovic, N.M.; Rossmeisl, J.; Greeley, J.; Norskov, J.K. Changing the activity of electrocatalysts for oxygen reduction by tuning the surface electronic structure. *Angewandte Chemie Int. Ed.* **2006**, *45*, 2897–2901. [\[CrossRef\]](#)
38. Xu, L.; Ge, Q. Effect of defects and dopants in graphene on hydrogen interaction in graphene-supported NaAlH₄. *Int. J. Hydrogen Energy* **2013**, *38*, 3670–3680. [\[CrossRef\]](#)
39. Zhang, J.; Wang, Z.; Zhu, Z.P. A Density Functional Theory Study on Mechanism of Electrochemical Oxygen Reduction on FeN₃-Graphene. *J. Electrochem. Soc.* **2015**, *162*, F1262–F1267. [\[CrossRef\]](#)

40. Qaseem, A.; Chen, F.Y.; Wu, X.Q.; Johnston, R.L. Pt-free silver nanoalloy electrocatalysts for oxygen reduction reaction in alkaline media. *Catal. Sci. Technol.* **2016**, *6*, 3317–3340. [\[CrossRef\]](#)
41. Roudgar, A.; Eikerling, M.; van Santen, R. Ab initio study of oxygen reduction mechanism at Pt-4 cluster. *Phys. Chem. Chem. Phys.* **2010**, *12*, 614–620. [\[CrossRef\]](#)
42. Fu, C.; Liu, C.; Li, T.; Zhang, X.; Wang, F.; Yang, J.; Jiang, Y.; Cui, P.; Li, H. DFT calculations: A powerful tool for better understanding of electrocatalytic oxygen reduction reactions on Pt-based metallic catalysts. *Comput. Mater. Sci.* **2019**, *170*, 109202. [\[CrossRef\]](#)
43. Lim, D.-H.; Wilcox, J. Mechanisms of the oxygen reduction reaction on defective graphene-supported Pt nanoparticles from first-principles. *J. Phys. Chem. C* **2012**, *116*, 3653–3660. [\[CrossRef\]](#)
44. Greeley, J.; Stephens, I.E.L.; Bondarenko, A.S.; Johansson, T.P.; Hansen, H.A.; Jaramillo, T.F.; Rossmeisl, J.; Chorkendorff, I.; Norskov, J.K. Alloys of platinum and early transition metals as oxygen reduction electrocatalysts. *Nat. Chem.* **2009**, *1*, 552–556. [\[CrossRef\]](#)
45. Liu, J.; Liu, H.; Chen, H.; Du, X.; Zhang, B.; Hong, Z.; Sun, S.; Wang, W. Progress and Challenges Toward the Rational Design of Oxygen Electrocatalysts Based on a Descriptor Approach. *Adv. Sci.* **2019**. [\[CrossRef\]](#)
46. Pasti, I.A.; Gavrilov, N.M.; Mentus, S.V. DFT study of chlorine adsorption on bimetallic surfaces—Case study of Pd3M and Pt3M alloy surfaces. *Electrochim. Acta* **2014**, *130*, 453–463. [\[CrossRef\]](#)
47. Hwang, S.J.; Kim, S.K.; Lee, J.G.; Lee, S.C.; Jang, J.H.; Kim, P.; Lim, T.H.; Sung, Y.E.; Yoo, S.J. Role of Electronic Perturbation in Stability and Activity of Pt-Based Alloy Nanocatalysts for Oxygen Reduction. *J. Am. Chem. Soc.* **2012**, *134*, 19508–19511. [\[CrossRef\]](#)
48. Karlberg, G.S.; Rossmeisl, J.; Norskov, J.K. Estimations of electric field effects on the oxygen reduction reaction based on the density functional theory. *Phys. Chem. Chem. Phys.* **2007**, *9*, 5158–5161. [\[CrossRef\]](#)
49. Tao, H.; Liu, S.; Luo, J.-L.; Choi, P.; Liu, Q.; Xu, Z. Descriptor of catalytic activity of metal sulfides for oxygen reduction reaction: A potential indicator for mineral flotation. *J. Mater. Chem. A* **2018**, *6*, 9650–9656. [\[CrossRef\]](#)
50. Xin, H.; Vojvodic, A.; Voss, J.; Norskov, J.K.; Abild-Pedersen, F. Effects of d-band shape on the surface reactivity of transition-metal alloys. *Phys. Rev. B* **2014**, *89*, 115114. [\[CrossRef\]](#)
51. Xie, Y.; Wang, Z.-W.; Zhu, T.-Y.; Shu, D.-J.; Hou, Z.-F.; Terakura, K. Breaking the scaling relations for oxygen reduction reaction on nitrogen-doped graphene by tensile strain. *Carbon* **2018**, *139*, 129–136. [\[CrossRef\]](#)
52. Yu, T.H.; Hofmann, T.; Sha, Y.; Merinov, B.V.; Myers, D.J.; Heske, C.; Goddard, W.A. Finding Correlations of the Oxygen Reduction Reaction Activity of Transition Metal Catalysts with Parameters Obtained from Quantum Mechanics. *J. Phys. Chem. C* **2013**, *117*, 26598–26607. [\[CrossRef\]](#)
53. Norskov, J.K.; Rossmeisl, J.; Logadottir, A.; Lindqvist, L.; Kitchin, J.R.; Bligaard, T.; Jonsson, H. Origin of the Overpotential for Oxygen Reduction at a Fuel-cell Cathode. *J. Phys. Chem. B* **2004**, *108*, 17886–17892. [\[CrossRef\]](#)
54. Hansen, H.A.; Viswanathan, V.; Norskov, J.K. Unifying Kinetic and Thermodynamic Analysis of 2 e(−) and 4 e(−) Reduction of Oxygen on Metal Surfaces. *J. Phys. Chem. C* **2014**, *118*, 6706–6718. [\[CrossRef\]](#)
55. Seitz, L.C.; Dickens, C.F.; Nishio, K.; Hikita, Y.; Montoya, J.; Doyle, A.; Kirk, C.; Vojvodic, A.; Hwang, H.Y.; Norskov, J.K.; et al. A highly active and stable IrOx/SrIrO3 catalyst for the oxygen evolution reaction. *Science* **2016**, *353*, 1011–1014. [\[CrossRef\]](#) [\[PubMed\]](#)
56. Kresse, G.; Furthmüller, J. Efficient iterative schemes for ab initio total-energy calculations using a plane-wave basis set. *Phys. Rev. B* **1996**, *54*, 11169–11186. [\[CrossRef\]](#) [\[PubMed\]](#)
57. Kresse, G.; Hafner, J. Ab initio molecular dynamics for liquid metals. *Phys. Rev. B* **1993**, *47*, 558–561. [\[CrossRef\]](#)
58. Blöchl, P.E.; Jepsen, O.; Andersen, O.K. Improved tetrahedron method for Brillouin-zone integrations. *Phys. Rev. B* **1994**, *49*, 16223. [\[CrossRef\]](#)
59. Perdew, J.P.; Burke, K.; Ernzerhof, M. Generalized gradient approximation made simple. *Phys. Rev. Lett.* **1996**, *77*, 3865–3868. [\[CrossRef\]](#)
60. Rossmeisl, J.; Karlberg, G.S.; Jaramillo, T.; Norskov, J.K. Steady state oxygen reduction and cyclic voltammetry. *Faraday Discuss.* **2008**, *140*, 337–346. [\[CrossRef\]](#)
61. Tripković, V.; Skúlason, E.; Siahrostami, S.; Nørskov, J.K.; Rossmeisl, J. The oxygen reduction reaction mechanism on Pt (111) from density functional theory calculations. *Electrochim. Acta* **2010**, *55*, 7975–7981. [\[CrossRef\]](#)

62. Johnson, R.D., III. *Computational Chemistry Comparison and Benchmark Database*; NIST Standard Reference Database Number 101; U.S. Secretary of Commerce; NIST: Gaithersburg, MD, USA, 2010; Volume 219, p. 611.
63. Henkelman, G.; Arnaldsson, A.; Jonsson, H. A fast and robust algorithm for Bader decomposition of charge density. *Comput. Mater. Sci.* **2006**, *36*, 354–360. [[CrossRef](#)]
64. Bader, R.F. *Atoms in Molecules: A Quantum Theory*; Oxford University Press: New York, NY, USA, 1990.
65. Seifitokaldani, A.; Savadogo, O.; Perrier, M. Density Functional Theory (DFT) Computation of the Oxygen Reduction Reaction (ORR) on Titanium Nitride (TiN) Surface. *Electrochim. Acta* **2014**, *141*, 25–32. [[CrossRef](#)]
66. Skulason, E.; Tripkovic, V.; Bjorketun, M.E.; Gudmundsdottir, S.; Karlberg, G.; Rossmeisl, J.; Bligaard, T.; Jonsson, H.; Norskov, J.K. Modeling the Electrochemical Hydrogen Oxidation and Evolution Reactions on the Basis of Density Functional Theory Calculations. *J. Phys. Chem. C* **2010**, *114*, 18182–18197. [[CrossRef](#)]



© 2020 by the authors. Licensee MDPI, Basel, Switzerland. This article is an open access article distributed under the terms and conditions of the Creative Commons Attribution (CC BY) license (<http://creativecommons.org/licenses/by/4.0/>).